Ceramics International 51 (2025) 48281–48294

Contents lists available at ScienceDirect

Ceramics International

journal homepage: www.elsevier.com/locate/ceramint

Channel-embedded porous zirconia surfaces to mimic dentine-cementum functionality in dental Implants: Design, production and characterisation

Manuela Proença [a,*], Joana Ribeiro [a], Paulo Pinto [a], Michael Gasik [c], Lia Rimondini [d], Filipe S. Silva [a,b], Sara Madeira [a,b]

[a] Center for Micro-Electro Mechanical Systems (CMEMS-UMinho), University of Minho, Campus de Azurém, 4800-058, Guimarães, Portugal
[b] LABBELS – Associate Laboratory, Braga, Guimarães, Portugal
[c] Department of Chemical and Metallurgical Engineering, School of Chemical Engineering, Aalto University Foundation, Aalto, Espoo, 00076, Finland
[d] Center for Translational Research on Autoimmune and Allergic Disease, CAAD, Department of Health Sciences, Università del Piemonte Orientale, Novara, 28100, Italy

ARTICLE INFO

Handling Editor: Dr P. Vincenzini

Keywords:
Cementum-like structure
PDL regeneration
Root-analogue dental implant
Porous zirconia surface

ABSTRACT

This study introduces a novel concept of dental implant integration, fibrointegration, which aims to replicate the natural attachment mechanism of teeth. To achieve this, zirconia samples featuring internal channels and one to three external porous layers were developed using Computer-Aided Design/Manufacturing (CAD/CAM) and dip-coating techniques, with the aim of mimicking the functional properties of natural teeth and thereby promoting the fibrointegration of a zirconia root-analogue implant. Results showed that the channel-embedded porous surfaces exhibited enhanced porosity, increased surface roughness, and superhydrophilic behaviour. Furthermore, the presence of microchannels induced a strong capillary effect, facilitating immediate fluid rise and spreading. The coating thickness increased with the number of dips, with the double-layer porous coating achieving an optimal thickness (≈100 μm), resembling natural cementum and exhibiting superior scratch resistance. These findings highlight the potential of bioinspired, channel-embedded porous zirconia surfaces to promote cell adhesion, guide growth, and stimulate fibrointegration, thereby improving implant stability.

1. Introduction

Dental implants play a vital role in modern dentistry, providing a reliable and long-lasting solution that restores oral function and aesthetics while significantly enhancing patients' quality of life. However, despite their success, implant failures occur, as osseointegrated implants lack several important functional components found in natural teeth, such as cementum and the periodontal ligament (PDL) [1,2]. These structures play a crucial role in buffering the forces of mastication, facilitating orthodontic tooth movement in conjunction with bone remodelling, and providing immunological defence [3–5]. Excessive occlusal load applied to a rigidly fixed dental implant, which lacks a PDL, directly transfers stress to the bone interface. This can lead to implant mobility, a key clinical sign of failure [6]. Furthermore, dental implants are more susceptible to infection due to the absence of the potential cellular defence mechanism of PDL, making them vulnerable to conditions like peri-implantitis, which can accelerate bone loss and compromise implant stability [7–9].

Various studies have shown that dental implants do not support the regeneration of periodontal tissues in fresh extraction sockets, even when the PDL is still intact [10–12]. While the remaining PDL can stimulate the formation of new PDL tissue between the implant and the surrounding alveolar bone, most of the collagen fibres are oriented parallel to the implant surfaces below the alveolar crest, which may compromise the functional integration of the implant. In contrast, autologous tooth roots with intact cementum and a remaining PDL can prevent osseointegration and help reconstruct the trilaminar structure of dentoalveolar fibrous joints within extraction sockets or prepared bony cavities [13]. Regenerating cementum is, therefore, essential to prevent the risk of implant fracture; however, it poses a challenge due to the unique structure and function of cementum [14]. It is an avascular and mineralised connective tissue, with about 45–50 % inorganic hydroxyapatite by weight and 50–55 % organic collagen (Type I) and non-collagenous matrix proteins and water by weight [15]. Several studies [16–18] have shown that cementum morphology has a porous matrix, however, its specific porosity and pore diameter are still poorly understood. Only a recent work demonstrated, through micro X-ray computed tomography, that human cementum presents an average pore diameter

* Corresponding author.
E-mail address: manuelaproenca12@gmail.com (M. Proença).

https://doi.org/10.1016/j.ceramint.2025.08.083
Received 18 June 2025; Received in revised form 4 August 2025; Accepted 7 August 2025
Available online 9 August 2025

of 26 ± 16 μm [19].

Zirconia is a promising metal-free alternative to titanium for dental implants, offering high mechanical strength, excellent biocompatibility, and effective osseointegration [20–22]. Its tooth-like colour enhances aesthetics by preventing gingival discolouration and visible roots, while its surfaces resist plaque accumulation, reducing peri-implant risks [23–25]. Furthermore, zirconia can be used to produce root-analogue implants [26,27]. They are customised for each patient and can be placed immediately after tooth extraction in a single-stage procedure. Their minimally invasive nature eliminates the need for bone drilling, sinus lifts, or bone augmentation [28]. Designed to fit precisely into the space left by the tooth root, these implants preserve the surrounding hard and soft tissues, promoting better healing and outcomes [29].

A potential strategy to induce tissue regeneration is the development of multiphasic biomaterials, or scaffolds, that replicate the structural and mechanical characteristics of natural oral soft and hard tissues [30–34]. These biomaterials can be combined with stem cells, which serve as a cellular source, and growth factors, which stimulate cell activity and promote tissue development. Notably, porous zirconia scaffolds have been successfully developed to support bone regeneration [30,35,36]. However, despite these advancements, the regeneration of the PDL in zirconia-based implants remains largely underexplored and poorly understood.

To address this challenge, biphasic (bone-PDL or PDL-cementum) [37–39] and triphasic (bone-PDL-cementum) [40,41] scaffold designs have been proposed to replicate the native hierarchical structure of the periodontium. Safi et al. [37] demonstrated that β-tricalcium phosphate (β-TCP)-coated titanium and zirconia implants could support periodontal tissue formation when covered with mesenchymal cell sheets derived either from PDL stem cells (PDLSCs) alone or from co-cultures of Bone Marrow Mesenchymal Stem Cells (BMMSCs) and PDLSCs. Proper cementum formation on the surfaces of the implants and the perpendicular insertion of PDL-like fibres into the cementum of the biohybrid implant were observed. Lee et al. [40] developed triphasic scaffolds with tissue-specific architectures that promoted the alignment of PDL-like fibres between bone-like tissue and cementum matrix protein positive regions. They printed polycaprolactone-hydroxylapatite (90:10 wt%) with microchannels of 100 μm for cementum, 600 μm for the PDL, and 300 μm for alveolar bone. More recently, anatomically shaped human molar and rat incisor scaffolds were also developed by 3D bioprinting from a poly-ε-caprolactone/hydroxyapatite composite with 200 μm interconnecting microchannels [42]. Stromal-derived factor-1 (SDF1) and bone morphogenetic protein-7 (BMP7) were delivered within these channels, promoting cell recruitment, regeneration of PDL, and new alveolar bone, supporting the effectiveness of cell homing.

The main objective of this work is to develop a novel implant surface that mimics the functional properties of natural teeth and promotes the fibrointegration of a zirconia root-analogue implant. Zirconia was selected as the base material due to its excellent biocompatibility and ability to be microstructured and functionalised, which properties that are crucial for supporting cell adhesion, proliferation, and extracellular matrix deposition. As illustrated in Fig. 1, the proposed strategy integrates internal microchannels, resembling dentinal microtubules, linking the interior (pulp cavity) to the exterior of the implant root, along with a porous layer on the implant surface to mimic cementum, ensuring secure anchorage of the fibres. This design would support the continuous nourishment of the periodontal fibres, promote their proper perpendicular orientation, and enhance their integration with the implant. Hence, to achieve this final goal, channelled zirconia specimens were produced using Computer-Aided Design/Computer-Aided Manufacturing (CAD/CAM) technology and dip-coated with single or multilayers of zirconia suspensions to replicate the functional characteristics of dental roots. Their microstructural and surface properties were investigated and compared to those of conventional zirconia dental implants, with a focus on their application in fibre-integrated root-analogue implants.

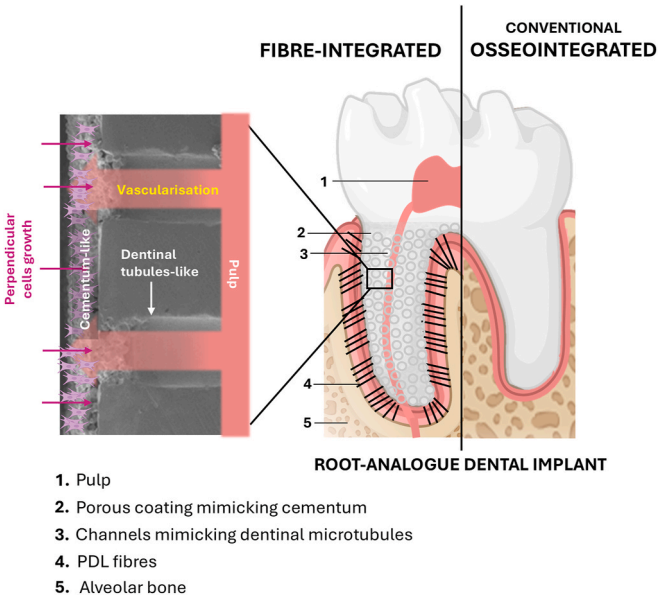

Fig. 1. Schematic representation of the principal differences between a new concept of fibre-integrated (left) and a conventional osseointegrated (right) root-analogue dental implant. In the fibre-integrated implant, vascularisation occurs from the inner side of the root-analogue implant (similar to pulp-dentine complex) to the outer side, which is coated with the cementum-like material and interfaces with fibroblasts, providing nutrients to them.

2. Experimental details

2.1. Production of the zirconia samples

In the present study, 9 different groups of 3 mol% yttria-stabilised zirconia (3Y-TZP) samples were manufactured and further characterised. The tested samples were channelled zirconia (C), channelled zirconia dip-coated with single (CD1) or multilayers of zirconia suspensions (CD2 and CD3) and standard zirconia dip-coated with single (D1) or multilayers of zirconia suspensions (D2 and D3). As-sintered zirconia (AS) and sandblasted zirconia (SB) were tested as control groups, representing the surfaces of commonly used dental implants.

2.1.1. Design and production of channelled zirconia specimens by CAD/CAM

A CAD/CAM system was used to manufacture the C samples with channels. The C design aimed to replicate dentinal microtubules function, thereby enabling internal vascularisation within the root-analogue implant. Thus, zirconia specimens (green state), with a diameter of 10 mm and height of 2 mm, featuring parallel microchannels each 0.40 mm in diameter (Ø) and spaced 0.70 mm apart, were modelled using *SolidWorks* software (Fig. 2 (a)).

The designed C specimens were fabricated starting from green compacted discs of 3Y-TZP (Dental Direkt), in a Roland DWX 50 CNC milling machine (Roland, 2011) presented in Fig. 2 (b). This 5-axis milling machine provides highly precise machining capabilities, featuring XYZ linear motion combined with rotational movement along the A and B axes. The A axis offers full 360° rotation, while the B axis enables tilting up to 20° forward or backward, ensuring exceptional flexibility for complex geometries. The machining process consisted of three operations: roughing, plunge milling, and peripheral milling. The roughing operation was performed using a flat-end mill with a 2 mm diameter to remove excess material until the sample reached a height of 2 mm. The plunge milling operation was carried out with a 0.4 mm diameter ball-end mill, using alternating Z-axis steps of 0.05 mm until the hole was fully through. The final peripheral milling operation involved stepwise milling with Z-axis increments of 0.3 mm using the

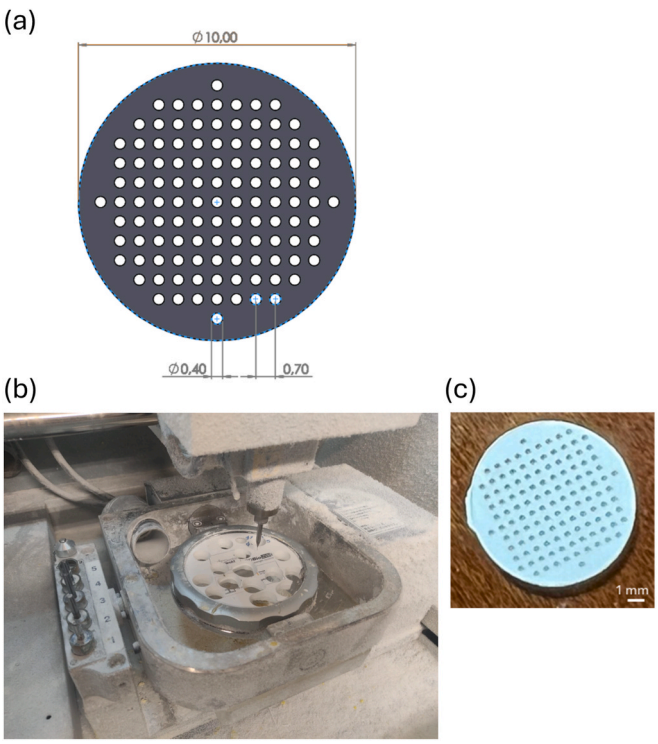

Fig. 2. Overview of the CAD/CAM system used in the manufacturing of channelled zirconia specimens: (a) CAD model and photographs of the (b) CAM system and the (c) channelled zirconia specimens in the green state. (For interpretation of the references to colour in this figure legend, the reader is referred to the Web version of this article.)

same tool as in the first operation, aiming to detach the sample from the zirconia block. The machining parameters for each operation are shown in Table 1.

Following the green machining stage, the C-specimens (Fig. 2 (c)) were sintered in a Zirkonofen 700 Ultra-Vakuum furnace from Zirkonzahn at 1500 °C for 2 h with a heating and cooling rate of 8 °C/min, following the manufacturer's recommendations. This temperature is commonly applied to ensure full densification of the ceramic while preserving a fine-grained tetragonal microstructure, which is essential for mechanical strength and transformation toughening, without altering the chemical composition [43,44]. After sintering, zirconia C-samples (8 mm diameter x 1.6 mm thick) were obtained, taking into account sintering shrinkage (≈20 %), as previously observed [30].

For comparison purposes, AS and SB samples - corresponding to as-sintered and sandblasted, respectively - were produced without channels. The AS samples were not subjected to any surface treatment, while the SB samples underwent sandblasting, replicating the treatment typically used for conventional implants. Both groups were fabricated using CAD/CAM technology, followed by a heat sintering process under the same conditions previously described. The SB samples were then treated using a blasting gun with alumina particles, each with a maximum size of 180 μm. A constant air pressure of 6 bar was applied for 20 s, with the nozzle positioned 7 cm from the surface being treated.

All samples were ultrasonically cleaned in isopropyl alcohol for 10 min and then in distilled water for 10 min to remove any loose debris or surface contamination.

2.1.2. Production of porous zirconia surfaces by dip-coating process

A biomimetic cementum material on implant surfaces is essential for replicating the function of human cementum and anchoring PDL fibres onto implant surfaces, both of which are critical for restoring periodontal functionality. In this context, porous zirconia surfaces were developed on the previously fabricated green zirconia specimens to mimic the porous structure of natural cementum.

For this study, a commercial powder of 3 mol% yttria-stabilised zirconia (TZ-3YSB-E, TOSOH Co., Japan) was used, consisting of spray-dried spherical granules with an average size of 45.08 ± 23.50 μm and a green density of 1.19 g/cm^3 (Fig. 3(a–i) and (a-ii)). This powder was employed in 2 distinct forms: fine and coarse, as illustrated in Fig. 4 (a), based on the methodology established by Roedel et al. [45]. The fine powder was prepared by sonicating the commercial powder (30 vol% solids in an aqueous medium) using a Hielscher UP200St ultrasonic probe for 1 min to break up agglomerates, resulting in particle sizes ranging from approximately 3 to 10 μm [45]. This powder was not subjected to heat treatment. In contrast, the coarse powder was produced through pre-sintering of the commercial powder, involving a heat treatment at 1150 °C for 1 h with a heating rate of 5 °C/min to consolidate the granules. Afterward, the material was sieved through a 60 μm mesh to obtain a narrower particle size distribution, resulting in an average particle size of 34.44 ± 14.66 μm, as shown in Fig. 3(b–i) and (b-ii)).

The powder mixture suspension was formulated in water with 30 vol % of solid content and 2 wt% of the dispersant agent - carboxymethylcellulose (CMC) - relative to the total solid mass. The solid content of the suspension consisted of a mixture of coarse and fine powders in a 4:1 vol ratio, considering an apparent density of 1.47 g/cm^3 of coarse powder. Fine powder was added to the suspension to increase the bonding strength between the coarse powder particles.

Dip-coating was performed on pre-fabricated zirconia specimens, both with and without channels, without applying any heat treatment (Fig. 4 (b)). The dip-coatings were made in a custom-made Dip Coater equipment, using a fixed speed of 4 mm/s and an immersion time of 5 s. Before each dip, one side of the specimen was coated with wax to mask the area and fill the microchannels, preventing it from being covered by the porous zirconia coating. The wax-coated side was intended to mimic the inner surface of dental roots (without cementum), while the uncoated side represented the outer surface (with cementum). The wax sublimed during each thermal treatment.

The layers were constructed on zirconia specimens following the sequence detailed below: initially, the specimens were dipped into a fine powder suspension to create a thin adhesive layer between the specimens and the subsequent powder mixture layer, followed by air drying for 20 min. Afterward, zirconia specimens, both with and without channels, were coated with 1 (D1 for specimens without channels, CD1 for specimens with channels), 2 (D2, CD2), or 3 (D3, CD3) layers of the same powder mixture suspension. This was achieved by performing 1, 2, or 3 dips, respectively, in the suspension, with a pre-sintering process at

Table 1
Machining parameters for each operation, including tool type, process type, cutting speeds in X/Y and Z directions, spindle speed and path interval.

Tool	Operation	X Y direction cutting speed (mm/min)	Z direction cutting speed (mm/min)	Spindle speed (rpm)	Z-axis depth increment (mm)
Ø 2.0 mm flat-end mill	Rough cutting	1500	150	20 000	0.30
Ø 0.40 mm ball end mill	Plunge milling	–	60	30 000	0.05
Ø 2.0 mm flat-end mill	Peripheral milling	1500	150	20 000	0.30

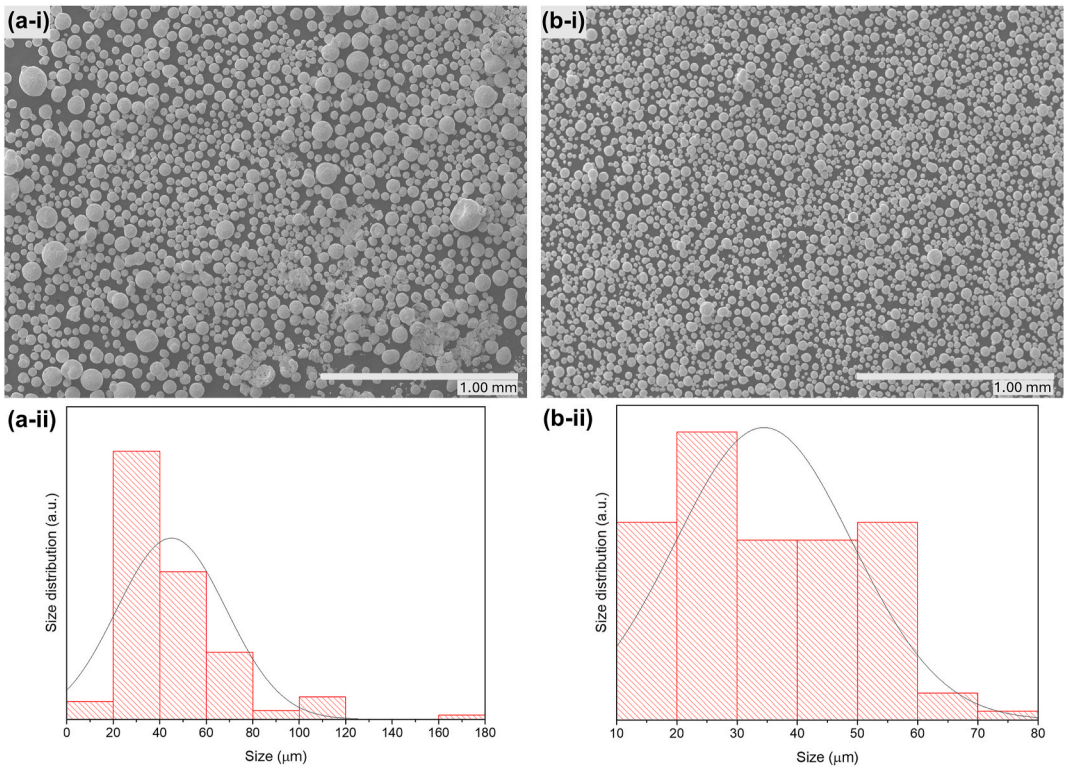

Fig. 3. Analysis of the particle size distribution for zirconia powders: (a) commercial powder and (b) coarse powder (≤60 μm). The corresponding top-view SEM micrographs are shown in (a–i) and (b–i), while the particle size distribution histograms are presented in (a-ii) and (b-ii).

1150 °C for 1 h between each dip. After applying the final layer, the specimens were air-dried for 20 min and then sintered in a conventional furnace at 1500 °C for 2 h.

For better clarity, Table 2 summarises the characteristics of the 9 different samples developed.

2.2. Microstructural analysis

The commercial zirconia, the coarse powder, and the microstructure of the different samples were analysed using Field Emission Gun Scanning Electron Microscopy (FEG-SEM) with a Hitachi FlexSEM1000II scanning electron microscope (Tokyo, Japan). The acquired top-view and cross-section images were analysed using ImageJ software to measure the average particle size of the powders, the average diameter of the channels and the average thickness of the porous zirconia surface. The main objective was to assess the uniformity of the channels, evaluate the increase in the thickness of the porous zirconia surface with successive dipping cycles, and examine the coverage of the channels surface achieved through successive coatings.

2.3. Density evaluation

The mean and relative densities of the samples were determined using the Archimedes displacement method. The dry weight of each specimen was first measured in air (m_{dry}), followed by the apparent weight when fully immersed in water ($m_{immersed}$). The bulk density (ρ_{bulk}) was then calculated using the following equation (1):

$$\rho_{bulk} = \frac{m_{dry}}{m_{dry} - m_{immersed}} \times \rho_{water} \quad (1)$$

where ρ_{water} is the density of water at room temperature. Each sample was measured four times. Porosity was then estimated based on the density measurements. The calculations assumed a water density of 1 g/cm^3 and a theoretical density of 6.05 g/cm^3 for 3 mol% yttria-stabilised zirconia after sintering [46,47].

2.4. Surface roughness measurements

To evaluate the surface roughness variations among the produced samples, surface roughness measurements were performed on the AS, SB and coated specimens without channels (D1-D3) using a contact profilometer (Surftest SJ 201, Mitutoyo, Tokyo, Japan). The profilometer was equipped with a sharp diamond stylus with a diameter of 2 μm. Four linear measurements were taken for each specimen over a measurement length of 5 mm at a speed of 0.5 mm/s. The evaluated roughness parameters included the average surface roughness (Ra) and the average maximum height of the profile (Rz).

2.5. Surface wettability and capillarity

The wettability of the zirconia sample surfaces was measured to evaluate their hydrophilicity. Increased surface hydrophilicity is expected to enhance interactions between the implant surface and the biological environment [48]. Therefore, contact angle measurements were performed for each group of samples to assess this. The sessile drop method was used to obtain the contact angles with an optical goniometer OCA 15 plus (DataPhysics, Germany). For the tests, droplets of ultrapure deionised water (at 18.2 Ohm) with a volume of 3 μL and a dosing rate of 5 μL/s were dispensed from a micrometric syringe. The sessile drop method was applied, and the contact angle was calculated using the SCA 20 software (DataPhysics Instruments GmbH). The behaviour of the droplets was video recorded with a frame rate of 52 frames per second at a resolution of 768 × 576 pixels. The experiments were conducted at room temperature (20 °C), and a minimum of four contact angle readings were taken on each sample, always at the same location (in the centre of the sample), immediately after the droplet reached the surface. It is important to highlight that before each measurement, all samples were ultrasonically cleaned in isopropyl alcohol

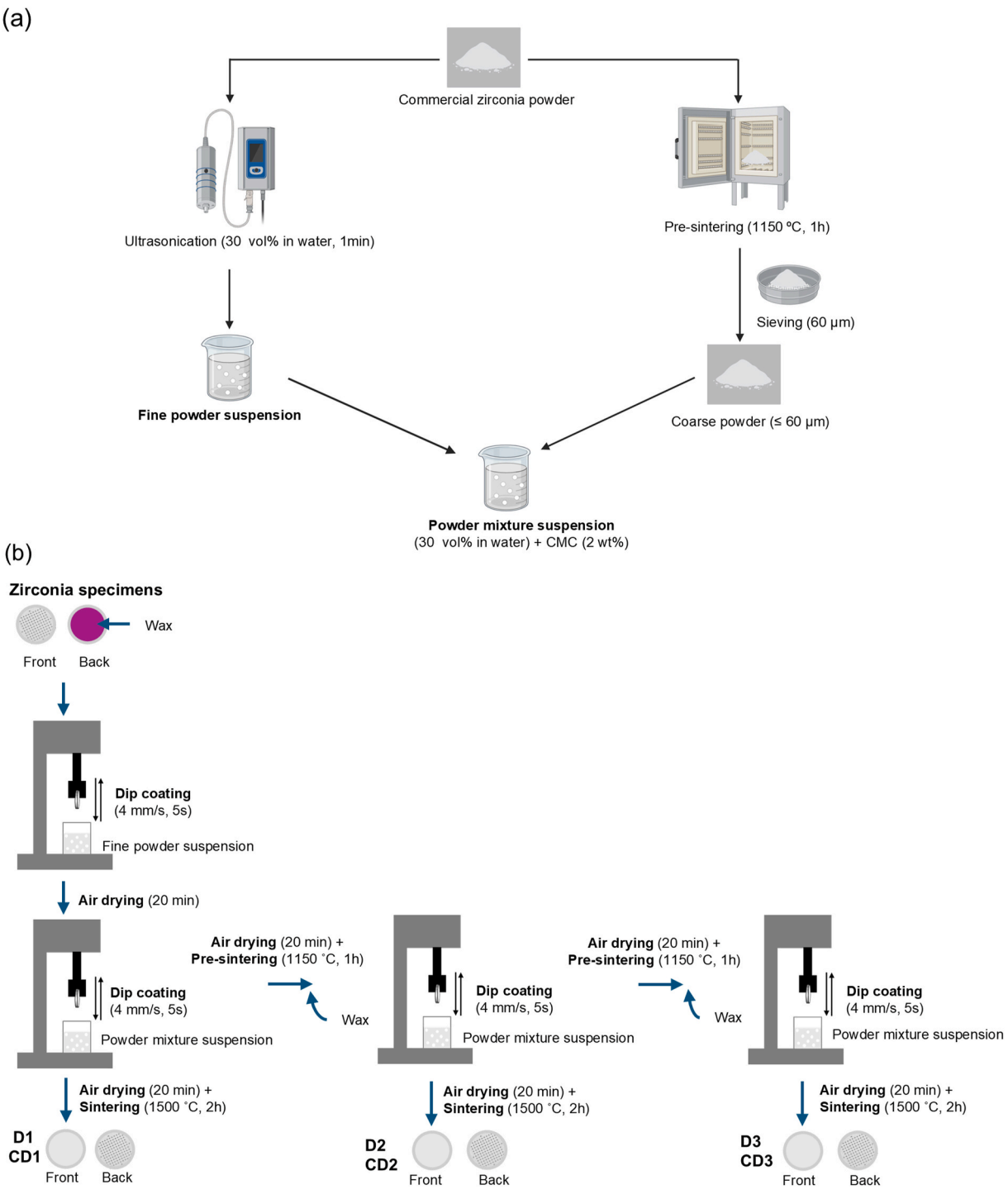

Fig. 4. Schematic illustration of (a) the production of fine powder and powder mixture suspensions, and (b) the dip-coating process used to produce D1-D3 and CD1⁻CD3 samples. D1–D3 correspond to standard zirconia substrates, while CD1–CD3 refer to channelled zirconia substrates.

for 1 min.

Also, capillarity, the spontaneous movement of fluids due to adhesive forces between the fluid and surrounding surfaces, is essential for the adsorption of biological fluids and the promotion of internal vascularisation within root-analogue implants. To evaluate the capillarity of the different samples, these were placed in contact with a phenol red aqueous solution while the fluid's ascent was documented through photography and the fluid rise time was measured. The red pigment was chosen to enhance visibility against the samples' opaque white background. This process enhances the implant's assimilation into the biological environment, promoting improved cellular attachment and nutrient cycling.

2.6. Scratch adhesion test

The adhesion of porous zirconia coating to the zirconia specimen after sintering was evaluated throughout the CSM Instruments Revetest scratch tester (Anton-Paar, Buch, Switzerland) equipped with a Rockwell diamond indenter, S-214, of 200 µm radius, friction force measurement, and an acoustic emission detector. The scratch tests were

Table 2
Zirconia samples description and fabrication method.

Samples designation	Description	Fabrication method
AS	Zirconia as-sintered (no surface treatment)	CAD/CAM
SB	Zirconia with sandblasting	CAD/CAM + Sandblasting
C	Zirconia with channels	CAD/CAM W/Channels
D1	Zirconia dip-coated with 1 layer	CAD/CAM + 1 Dip-Coating
D2	Zirconia dip-coated with 2 layers	CAD/CAM + 2 Dip-Coating
D3	Zirconia dip-coated with 3 layer3	CAD/CAM + 3 Dip-Coating
CD1	Zirconia with channels and dip-coated with 1 layer	CAD/CAM W/Channels + 1 Dip-Coating
CD2	Zirconia with channels and dip-coated with 2 layers	CAD/CAM W/Channels + 2 Dip-Coatings
CD3	Zirconia with channels and dip-coated with 3 layers	CAD/CAM W/Channels + 3 Dip-Coatings

performed by applying a progressive (≈linearly increasing) load of 100 N/min from 1 to 100 N over a length of 3 mm, according to ISO 20502:2005. Two critical load values were registered to provide a better understanding of the coating behaviour: L_{C1} and L_{C2}, which represent the smallest loads at which recognisable failures occur. In the lower load range, the induced stresses lead to phenomena such as conformal or tensile cracking of the surface, while the material remains intact and compact. This marks the first critical load (L_{C1}), associated with the appearance of the first minor crack or change in surface topology. At higher loads, another critical point, L_{C2}, is defined. This corresponds to the onset of material detachment through mechanisms like spalling and chipping, indicating a large-scale coating detachment or peeling. These two critical loads serve as key indicators of the material's behaviour under stress. Critical loads were determined by analysing the scratch track using optical microscopy after the scratch test [49].

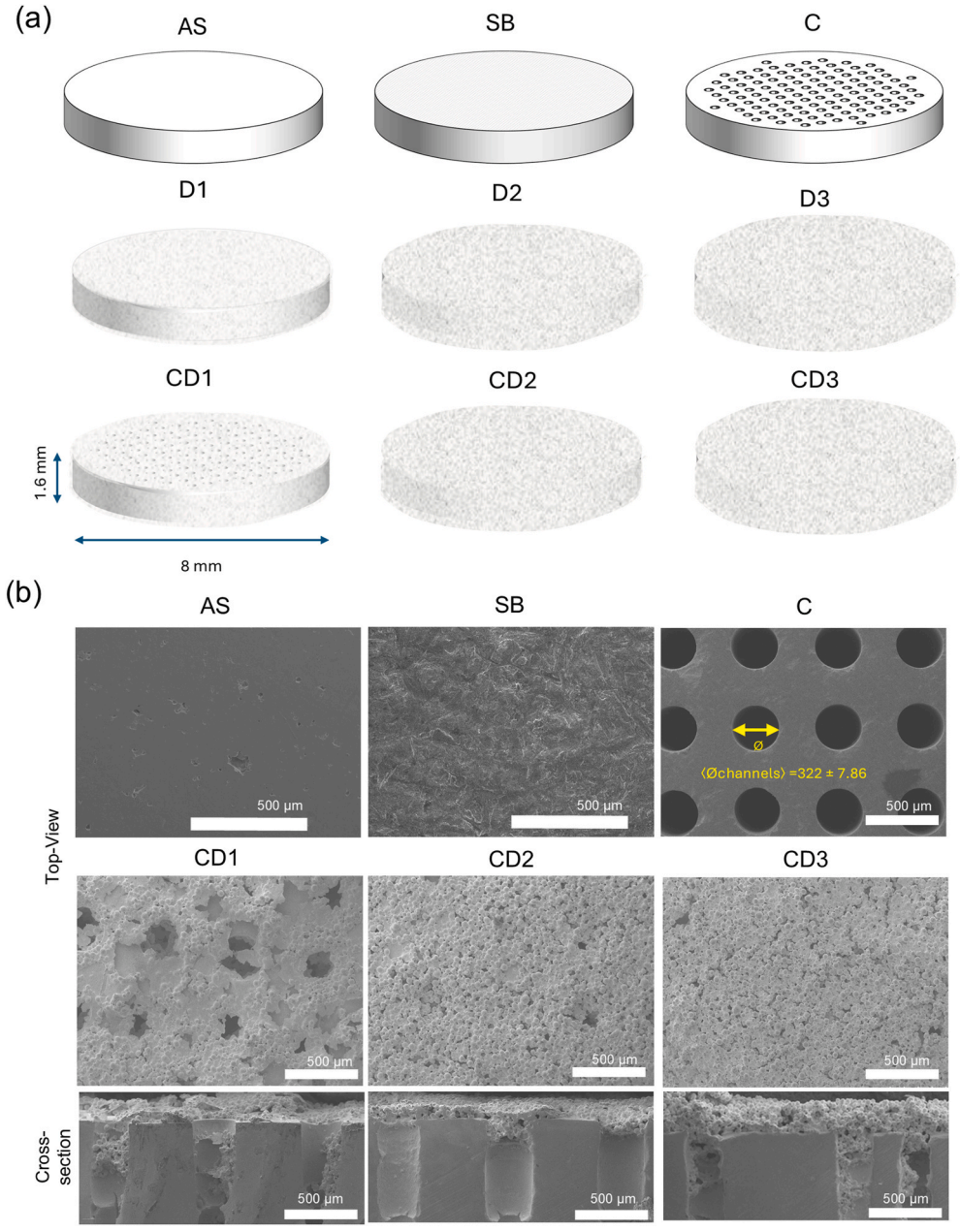

Fig. 5. (a) Schematic representation and (b) top-view SEM micrographs of the produced samples, along with cross-sectional SEM micrographs of the CD1, CD2, and CD3 samples, showing microchannels.

3. Results and discussion

3.1. Microstructural characterisation

The potential of zirconia to facilitate PDL regeneration is closely linked to its physicochemical properties and the way its surface can be designed and functionalised to mimic natural periodontal structures. Zirconia exhibits excellent biocompatibility and low cytotoxicity, which are essential for the adhesion and proliferation of periodontal cells. In addition, surface modifications, such as microstructuring, porosity, and incorporation of biomimetic features, can modulate cell behaviour and promote tissue-specific responses. In the present study, the incorporation of internal microchannels, resembling dentinal tubules, and porous outer coatings, mimicking cementum, aimed to recreate the structural cues required for fibre anchorage and orientation. The porous coating may provide not only physical interlocking but also a suitable environment for cellular infiltration and extracellular matrix deposition. Moreover, the microchannels can facilitate fluid exchange, contributing to nutrient transport and potentially supporting early vascularisation within the implant–tissue interface. Altogether, these bioinspired features are intended to guide the formation and perpendicular orientation of PDL-like fibres, thereby enhancing fibrointegration and mimicking the natural tooth–periodontium attachment mechanism.

Fig. 5 (a) and (b) provide a schematic representation and top-view SEM micrographs of the produced samples, along with cross-sectional SEM micrographs for the CD1^{-}CD3 samples, respectively. As expected, the surface microstructure (Fig. 5(b)) of the sample C, closely resembles that of the AS sample, with the primary distinction being the presence of channels. The channel diameter (Ø) was measured and compared to the dimensions specified in the CAD model. The average channel diameter (<Øchannel>) was found to be 322 ± 7.86 μm, indicating a high degree of size uniformity. This value is approximately 20 % smaller than the designed value, likely due to shrinkage during the sintering process [30].

For the samples coated with the porous zirconia layer (CD1^{-}CD3), the top-view micrographs (Fig. 5 (b)) clearly illustrate the effect of the number of dips. A single dip was insufficient to cover the substrate channels, showing only a thin zirconia layer composed of fine powder particles and a few coarse powder particles on the surface. This is likely due to the channels' small size and the coating's viscosity, which creates surface tension that prevents the coating from penetrating effectively. In contrast, 2 and 3 dips achieved complete coverage of the channels, with an increase in particle density observed from 2 to 3 dips. Here, the beneficial effect of the fine powder particles is clearly evident in their role in establishing bonds between the coarser powder particles. Despite the use of wax to seal the channels, cross-sectional images of the CD1^{-}CD3 samples (Fig. 5 (b)) reveal the presence of particles in the initial segments of certain channels. However, only a few zirconia particles adhered to the walls, leaving the channels largely unobstructed, thereby allowing capillary action to occur. This will enable fluid to flow from the inner side of the root-analogue implant (similar to pulp-dentine complex) to the outer side, which is coated with the cementum mimetic material and interfaces with fibroblasts, serving as their source of nourishment, as illustrated in Fig. 1.

The effect of the number of dips is also visible on the coating thickness. The thickness (d) values measured on the CD1^{-}CD3 samples were recorded, and their average thickness are exhibited in Fig. 6. The coating thickness was found to vary linearly with the number of dips for the samples CD1 and CD2, varying from 99.87 ± 43.39 μm to 167.04 ± 51.87 μm, respectively. However, the CD3 sample, in turn, shows an average thickness of 502.01 ± 108.75 μm, which is a value higher than expected, presenting also a bigger scatter in thickness values. This may be caused by insufficient time for the liquid to penetrate the surface porosity, coupled with the viscosity of the suspension, resulting in the formation of heterogeneities in the coating layer.

Considering that the acellular cementum thickness can range from 50 to 200 μm, depending on age [50], it can be inferred that the CD2 sample exhibits a morphology most similar to that of natural cementum.

3.2. Density characterisation

The density and porosity of a biomimetic material are essential factors that deeply affect its functionality and ability to integrate biologically [51]. Therefore, the mean density, relative density, and porosity of the produced samples were determined, with the results presented in Fig. 7 (a).

The measured mean densities of the AS and the SB samples were 5.78 ± 0.11 g/cm^3 and 6.05 ± 0.08 g/cm^3, respectively. These values are close to the theoretical density of 3mol% yttria-stabilised zirconia (≈6.05 g/cm^3), confirming good densification and low porosity, in

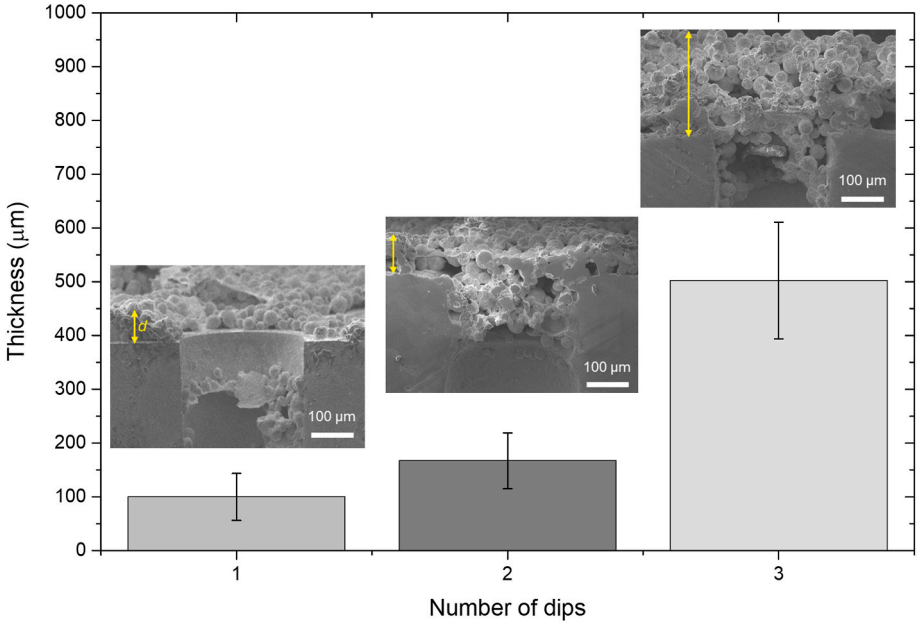

Fig. 6. Average thickness of the zirconia porous layers as a function of the number of dips.

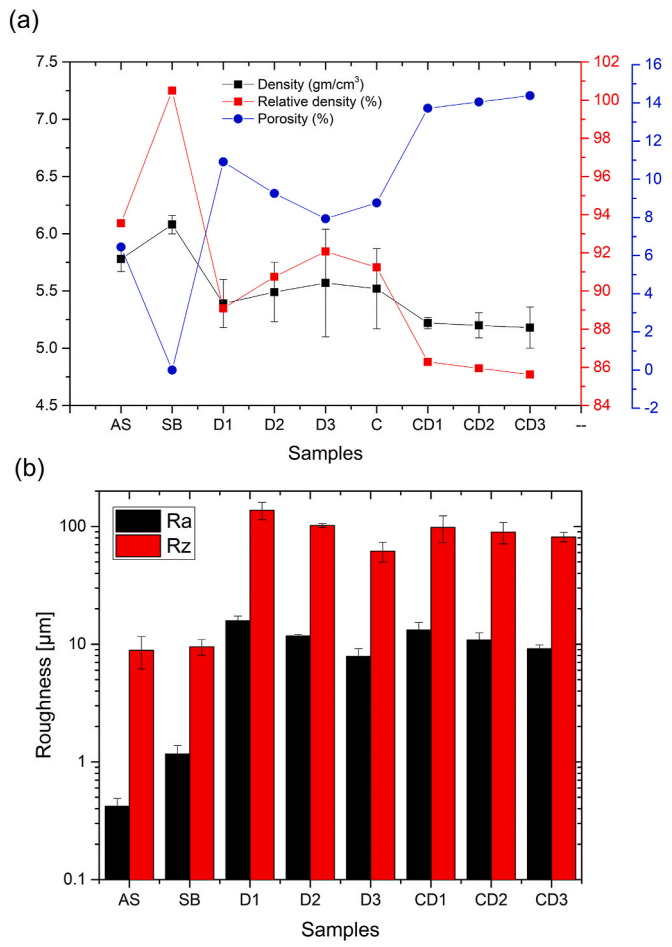

Fig. 7. (a) Average density, relative density and porosity and (b) average surface roughness (Ra) and average maximum profile (Rz) of the produced samples.

agreement with values reported in the literature [46]. However, the density of samples with channels (sample C) decreases to 5.52 ± 0.05 g/cm^3, while samples with porous zirconia coatings (sample D1-D3) show a decrease to 5.39 ± 0.21 g/cm^3 (D1), 5.49 ± 0.26 g/cm^3 (D2) and 5.57 ± 0.47 89 % g/cm^3 (D3). This increased their relative porosity, reaching 9 % for sample C, 11 % for sample D1, 9 % (D2) and 8 % (D3), as shown in Fig. 7 (a). These changes are attributed to an increase in the number of voids within the samples and a reduction in the volume of solid material. Several studies have reported that an increase in the number or volume fraction of pores leads to a corresponding decrease in the bulk density of zirconia-based materials [52,53]. The decrease in density becomes even more pronounced in samples featuring both channels and coatings (CD1$^-$CD3), with density values dropping to 5.22 ± 0.05 g/cm^3 in sample CD1, 5.20 ± 0.11 g/cm^3 in CD2, and 5.18 ± 0.18 g/cm^3 in CD3. This reduction in density corresponds to an increase in porosity to about 14 %. However, no significant differences were observed between the samples with varying numbers of dips, as indicated in Fig. 7 (a), likely due to the large variability in density values.

In natural tooth roots, the porosity of dentine ranges from 1 % to 32 % [54], facilitating fluid movement that is essential for nutrient delivery and waste exchange within the pulp-dentine complex. While the precise porosity of cementum remains largely unknown, it plays a vital role in supporting the attachment of PDL fibres and anchoring the tooth within its socket [55]. Given that the produced CD1$^-$CD3 samples exhibit a porosity of approximately 14 %, it can be inferred that their porosity closely resembles that of natural tooth roots. This similarity in porosity may further enhance their potential to achieve functional and mechanical equivalence.

3.3. Surface analysis

3.3.1. Roughness results

The interaction of the tissues can be altered by the physical-chemical characteristics of the surface, such as the presence or not of roughness on the surface of the dental implants. Therefore, surface roughness measurements were carried out to evaluate the differences between the produced samples. Fig. 7 (b) shows the evaluated roughness parameters - average surface roughness (Ra) and average maximum height of the profile (Rz).

As shown in Fig. 7 (b), the AS and the SB zirconia specimens exhibited significantly lower average Ra and Rz values compared to the coated samples. Specifically, the AS samples had average Ra and Rz values of 0.42 ± 0.07 µm and 8.87 ± 2.71 µm, respectively, indicating their dense and nearly homogeneous microstructure. After sandblasting treatment, a slight increase in both Ra and Rz values was observed, with average values of 1.17 ± 0.21 µm and 9.50 ± 1.46 µm, respectively, which is consistent with previous studies [56,57]. However, the coated zirconia samples (D and CD) displayed an even greater increase in roughness, probably due to the presence of the coating, .and increase of the samples' porosity, as verify in Fig. 7 (a).

The roughness parameters decrease with an increasing number of dips for both D and CD samples. The D1 sample exhibited average Ra and Rz values of 15.79 ± 1.54 µm and 137.3 ± 23.09 µm, respectively, while the D3 sample showed reduced average Ra and Rz values of 7.87 ± 1.27 µm and 61.73 ± 11.89 µm, respectively. For the CD samples, the average Ra and Rz values decrease from 13.22 ± 2.11 µm and 98.1 ± 25.18 µm, respectively, in the CD1 sample, to 9.14 ± 0.69 µm and 81.39 ± 7.52 µm, in the CD3 sample. The decrease in roughness values as the number of dips increases could be attributed to the coating densification and consolidation. With each dip, the coating may form a more cohesive and continuous layer, which could fill in any surface irregularities or roughness from previous layers. This could result in a smoother surface, as the microparticles within the coating become more closely packed, reducing the overall roughness.

Previous works suggested a positive correlation between surface roughness and cellular attachment and cell proliferation [58]. Osteoblasts and fibroblasts generally proliferate and differentiate better on rougher surfaces that offer more anchorage points for cell attachment, whereas smooth zirconia may not support these processes as effectively [57,59,60]. Hence, fibroblast cells' adhesion and proliferation are expected to be higher in the coated specimens with very rough surfaces than in the AS and SB samples. However, the degree of roughness must be optimised—moderate roughness typically offers the best balance, promoting cell adhesion and proliferation without increasing the risk of bacterial colonisation or inflammation.

To complement the previous analysis, Fig. 8 illustrates the correlation between the number of dip-coated layers and the density, porosity, and roughness for both D1-D3 and CD1$^-$CD3 zirconia samples. In D1-D3 samples (Fig. 8 (a)), a clear linear increase in density is observed with additional coating layers, accompanied by a significant reduction in porosity and surface roughness. These trends reflect a progressive densification of the coating, likely due to the effective packing of particles over a flat substrate without internal geometry constraints.

In contrast, the CD1$^-$CD3 zirconia samples (Fig. 8 (b)) exhibited an inverse behaviour: density slightly decreased with more coatings, while porosity increased and roughness decreased at a slower rate. The observed trends may be attributed to capillary-driven effects and the influence of internal channel geometry, which could restrict uniform particle deposition and promote a more porous and heterogeneous microstructure.

The linear regression equations included in the figure confirm these behaviours, revealing high R^2 values in all cases and supporting the relevance of geometry in determining the final coating characteristics.

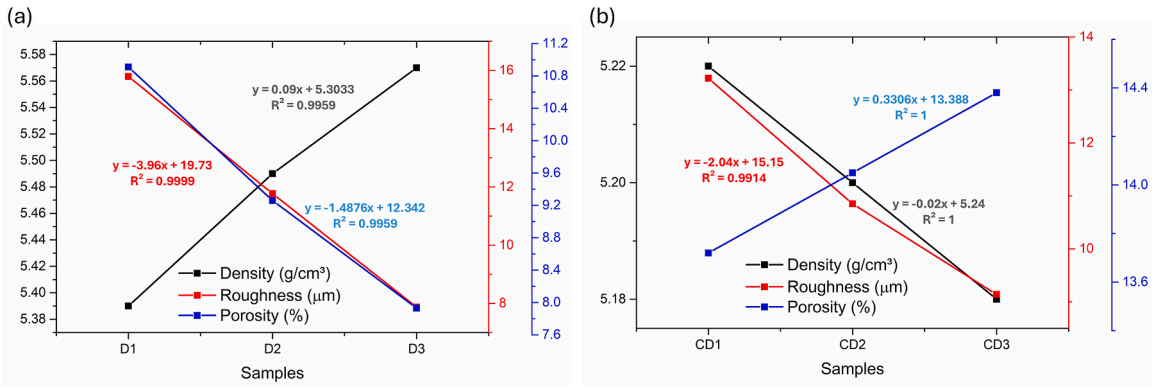

Fig. 8. Correlation between the number of dip-coated layers and density (black), roughness (red), and porosity (blue) for (a) D1-D3 and (b) CD1¯CD3 samples. Linear trendlines with corresponding equations and R^2 values are shown for each property. (For interpretation of the references to colour in this figure legend, the reader is referred to the Web version of this article.)

3.3.2. *Wettability and capillarity results*

The surface wettability of biomaterials influences the sequence of biological events that occur at the interface between the biomaterial and the host [48]. More specifically, the wettability of the material plays a crucial role in protein adsorption, which in turn affects cell adhesion and improves tissue integration.

This study evaluated the surface wettability of all samples' surfaces using the water contact angle measured when the droplet touched the surface. Literature reports that a surface is classified as hydrophilic when the contact angle is less than 90°, and as hydrophobic when it exceeds 90°. Super-hydrophilic and super-hydrophobic behaviours are observed at contact angles below 5° and above 150°, respectively [48,61]. Sample images of droplets and average contact angle measurements are shown in Figs. 9 and 10, respectively.

After analysing the results (Fig. 10), it can be concluded that all samples exhibit a water contact angle below 90°, indicating their hydrophilic character. The AS samples presented a measured contact angle of 50.06 ± 7.88°, which indicates that zirconia material exhibits a great water-spreading ability (hydrophilic nature), as previously reported in the literature [57,62]. Moreover, the results show that the various production and treatment methods of zirconia surfaces can affect their wettability in different ways. Although no significant differences were observed between them, the increased surface roughness in SB samples (Fig. 7 (b)) appears to lead to a higher average contact angle (71.50 ± 6.84°) compared to the smooth AS surface. These findings are, once again, supported by results from similar studies [63]. On the other hand, the introduction of microchannels (Sample C) resulted in a slight reduction of the water contact angle to 48.28 ± 4.04°. Notably, within 2 s of contact with the surface, the water completely penetrated the channels, reducing the contact angle to 0°. This transition indicates that

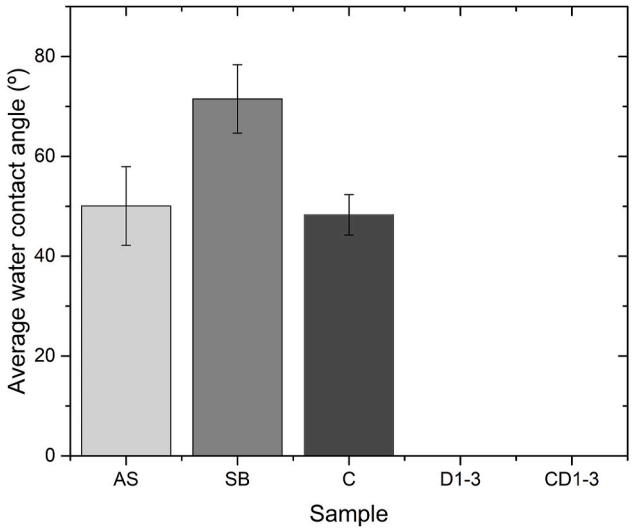

Fig. 10. Average water contact angle (°) measurements of the produced samples.

Fig. 9. Images of water droplets on the surfaces of the produced samples.

the surface's wettability shifted from hydrophilic to superhydrophilic, facilitating rapid water infiltration into the microchannels.

A substantial improvement in wettability was also observed in the coated specimens (CD1¯CD3 and D1-D3) due to the physical modifications induced by the porous zirconia coating on the zirconia surface. The water contact angle for all coated specimens was measured at 0°, demonstrating superhydrophilic behaviour. This can be attributed to the porous coating on the surface and consequently high surface roughness (Fig. 7 (b)). It provides a significantly larger surface area for interaction with water, allowing more water to spread across the surface, and thereby reducing the contact angle.

As stated before, implants with hydrophilic surfaces enhance the initial interactions between the surface and the body fluids, which is relevant for wound healing and osseointegration [64]. Nevertheless, recent works has demonstrated that superhydrophilic coatings promoted fibroblasts adhesion and can be attached perpendicularly to the superhydrophilic surface [65,66]. Hence, like natural cementum [15], CD1¯CD3 samples are expected to be favourable for fibroblast cells' adhesion and attachment.

The main goal of integrating microchannels in the zirconia was to induce and facilitate the infiltration and supply of nutrients and fluids within root-analogue dental implants. In this sense, the capillarity of the microchannels was assessed by means of a qualitative analysis, where a red pigment was evaluated. With this analysis authors intended to find out if the microchannels depth and width presented capillarity effect.

Fig. 11 shows the tested samples after contact with the red pigment. As expected, zirconia samples without channels (Fig. 11 (a) and (c)) failed to promote the desired capillary effect. In contrast, the incorporation of microchannels effectively induced fluid rise immediately upon contact with the pigment, as evidenced by the reddish colour present at the top of the channels in Fig. 11 (b). Furthermore, within 4 s of contact, the red pigment spread across the entire surface of the sample with both channels and the porous coating (Fig. 11 (c)). These results suggest that fluid molecules adhere to the zirconia surface, while cohesive forces among them drive the fluid through the narrow channels [67]. Additionally, the presence of a porous zirconia coating facilitates fluid distribution, potentially enhancing PDL attachment.

3.4. scratch adhesion test

This test was carried out to evaluate the adhesion strength of porous zirconia coating on the zirconia substrate and to assess if porous zirconia detachment takes place under implantation stress conditions. In this work, a progressive load varying from 1 to 100 N was applied, taking into account implantation conditions (considering dental implants insertion torque 35–50 Ncm routinely applied, but also extreme conditions (high insertion torque >50 Ncm to full study the novel developed surface [68]. The characteristic results of the scratch tests, in terms of L_{C1} and L_{C2}, are presented for the D1-D3 and CD1¯CD3 samples in Table 3. Fig. 12 (a) shows the plots of the evolution of frictional force (Ft), acoustic emission (AE), and penetration depth (Pd) as a function of the progressively applied normal load (Fn) for the D1-D3 and CD1¯CD3 samples, while Fig. 12 (b) presents the corresponding optical microscopy micrographs after progressive scratch.

Considering the comparable surface morphology of the samples, it is rather clear that there are no significant differences in L_{C1} values, which all fall within the same range (0–20 N). However, determining the exact L_{C1} value for each sample proved to be challenging, as both the friction force and acoustic emission curves exhibited irregular behaviour right from the start of the test.(Fig. 12 (a)). This behaviour is attributed to the strong influence of surface morphology on acoustic emission signals [69]. Due to the rather high surface roughness of the dip-coated samples, small cracks form immediately upon the initial contact between surface asperities and the indenter tip (Fig. 12 (b)), leading to cohesive failure and drastic variations recorded by the acoustic emission detector.

Regarding the second critical load (L_{C2}) values, Table 3 shows that an increasing number of dips generally results in a rise in L_{C2}, thereby delaying the onset of adhesive failure, with the exception of the CD3 sample. This trend is likely attributed to the increased thickness of the samples, with L_{C2} values ranging from 26.37 N (D1) to 36.91 N (D2) and 40.53 N (D3), and from 52.02 N (CD1) to 59.84 N (DC2) and 48.24 N (DC3). Notably, the samples with channels exhibit higher critical loads than those without channels, potentially because the channels introduce greater irregularities in thickness, resulting in locally thicker regions. In all samples, both penetration depth and frictional force increase progressively with the applied normal load (Fig. 12 (a)). However, a sharp drop in both parameters is observed at loads that lead to porous coating detachment or substrate exposure, as shown in Fig. 12 (b), marking the occurrence of adhesive failure. While partial coating detachment is

Table 3
Critical load values for the D1-D3 and CD1¯CD3 samples.

Samples	L_{C1} (N)	L_{C2} (N)
D1	0–20	26.37
D2		36.91
D3		40.53
CD1		52.02
CD2		59.84
CD3		48.24

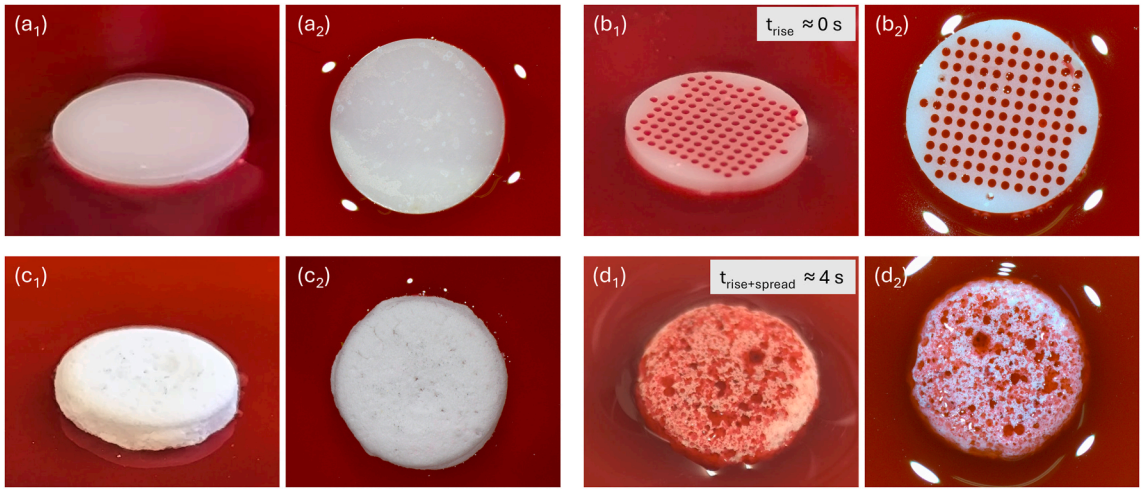

Fig. 11. Representative images of the fluid rise in the samples: (a) AS; (b) C; (c) D2; (d) CD2 in front ($_1$) and top view ($_2$).

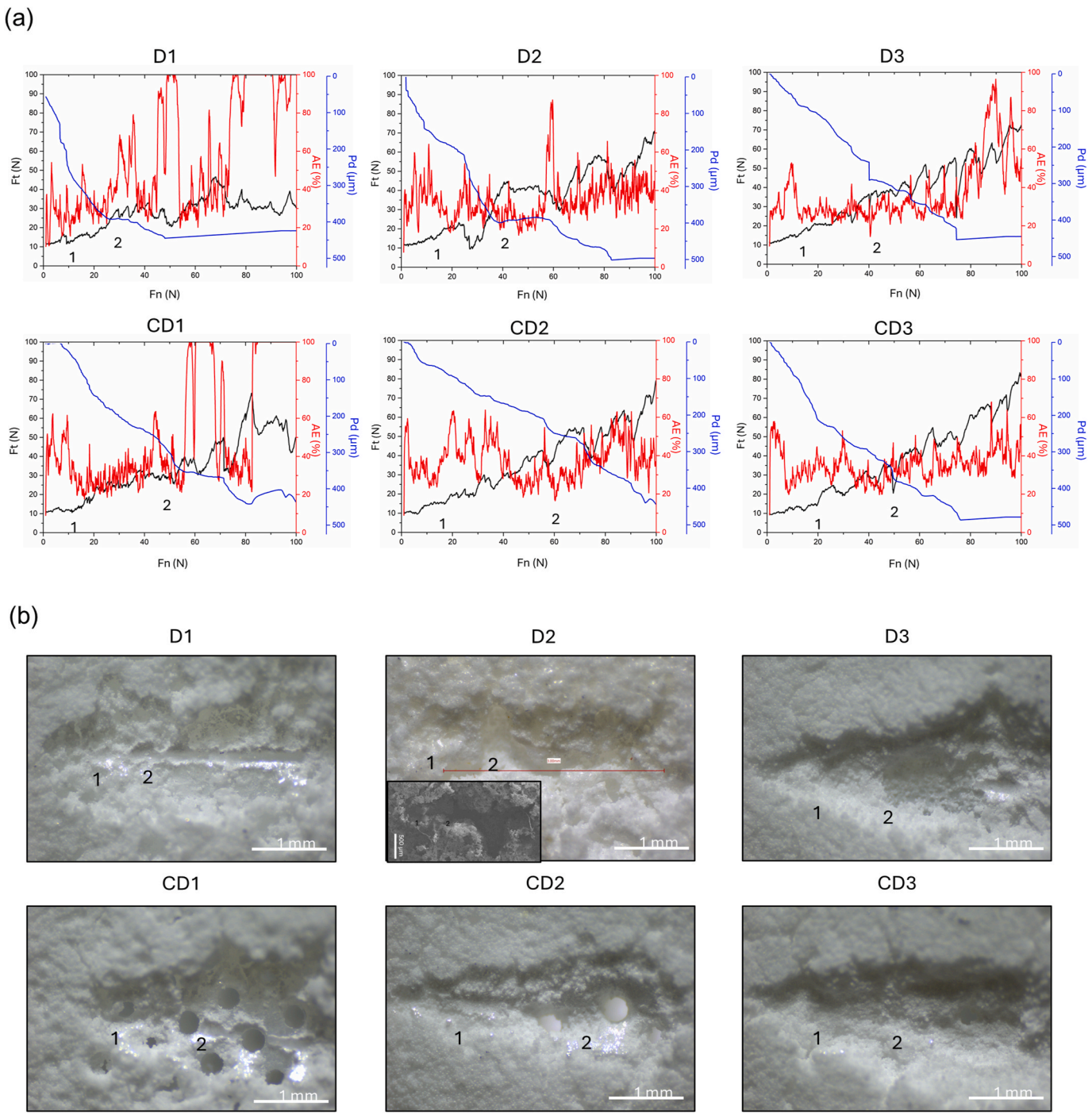

Fig. 12. Scratch test on D1-D3 and CD1¯CD3 samples. (a) Variation of frictional force (Ft), acoustic emission (AE), and penetration depth (Pd) as a function of the progressively applied normal load (Fn). (b) Optical images of the surfaces of the samples after the progressive scratch test. The critical loads, LC1 and LC2, are denoted as 1 and 2, respectively.

evident in the D2, D3, CD2, and CD3 samples at the second critical load (Fig. 12 (b)), substrate exposure and deformation of the compact zirconia are clearly visible in the D1 and CD1 samples due to their thinner thickness. This observation is further supported by the presence of more intense acoustic emission peaks (Fig. 12 (a)) in the D1 and CD1 samples, confirming the exposure of a different material beneath the coating.

The second critical load value for the porous zirconia coating is lower than those reported in studies on zirconia coatings deposited by plasma spray [70] and sintered by hot pressing [71] (approximately 70 N), but it is similar to the value observed in a study performed by Ref. [49] on micropatterned silica coatings. Hence, given the porous structure of the coating, which is markedly different from the compact structure of the substrate, it can be concluded that good adhesion has been achieved between the porous zirconia coating and the zirconia substrate with channels, particularly for the CD2 and CD3 samples. As a result, the coating exhibits high scratch resistance. Therefore, under implantation conditions, some cohesive failures are expected for CD2 and CD3 samples due to the material's elastic properties. However, the coating-substrate interface remains intact and is not compromised.

Fig. 13 provides a comprehensive visualisation of the results, revealing that coating thickness, density, surface roughness, and scratch resistance are interdependent. The analysis reveals a clear inverse

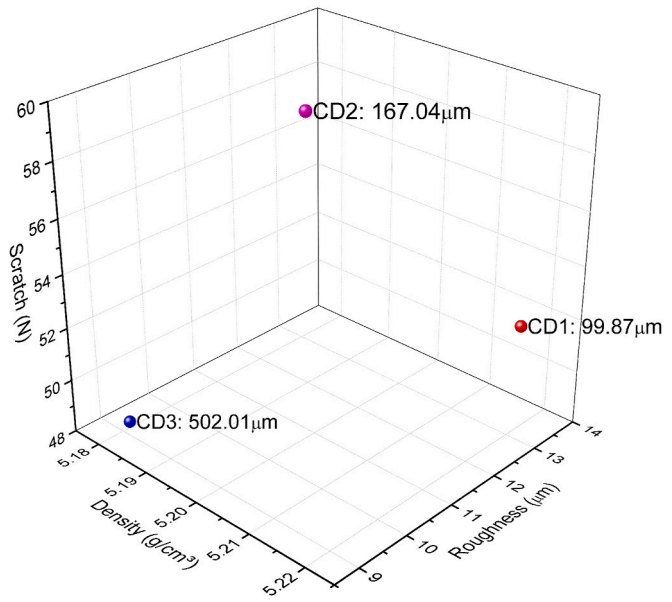

Figs. 13. 3D scatter plot representing the correlation between density, surface roughness (Ra), and critical load (LC2) for CD1, CD2, and CD3 samples. Each data point is labelled with the sample name and corresponding coating thickness.

relationship between coating thickness and surface roughness, with CD3 exhibiting the highest thickness and the lowest Ra value, while CD1 shows the opposite trend. Despite minor differences in density among the samples, the critical load (LC2) varies more significantly. Notably, CD2, with an intermediate thickness and roughness, achieved the highest scratch resistance. This suggests that moderate coating thickness combined with controlled roughness may optimize mechanical performance under scratch testing conditions.

4. Conclusions

This study introduces a novel strategy for promoting dental implant fibrointegration by the developing of channel-embedded porous zirconia surfaces. The channelled samples were successfully produced by CAD/CAM and dip-coated with one to three zirconia layers (CD1⁻CD3 samples). Their microstructural and surface properties were assessed and compared to conventional implants (AS and SB samples). The findings support several key conclusions.

- The CAD/CAM process successfully produced uniform microchannels.
- The coating thickness increased with the number of dips, with CD2 aligning best with natural acellular cementum (50–200 μm).
- Dip-coated samples exhibited enhanced porosity compared to the AS and SB samples, leading to higher surface roughness and improved wettability—showing a superhydrophilic behaviour. Furthermore, microchannels induced a strong capillary effect, with samples showing immediate fluid rise and spreading, unlike those without channels. These properties are essential for protein adsorption, cell adhesion, and tissue integration, which are key factors in promoting fibroblast attachment and PDL integration.
- Contrary to CD1, CD2 and CD3 showed high scratch resistance, maintaining an intact coating-substrate interface under implantation conditions.

In conclusion, channel-embedded porous zirconia surfaces—particularly the double-layer configuration—demonstrate significant potential to promote fibrointegration by emulating the natural function of a tooth's root. This bioinspired design promises enhanced implant stability and soft tissue integration. Future in vitro studies are essential to assess cellular responses and further refine the implant's biological performance.

CRediT authorship contribution statement

Manuela Proença: Writing – original draft, Investigation, Formal analysis. **Joana Ribeiro:** Investigation, Formal analysis. **Paulo Pinto:** Investigation, Formal analysis. **Michael Gasik:** Writing – review & editing, Conceptualization. **Lia Rimondini:** Writing – review & editing, Conceptualization. **Filipe S. Silva:** Writing – review & editing, Supervision, Resources, Project administration, Funding acquisition, Conceptualization. **Sara Madeira:** Writing – review & editing, Supervision, Resources, Project administration, Investigation, Funding acquisition, Conceptualization.

Declaration of competing interest

The authors declare that they have no known competing financial interests or personal relationships that could have appeared to influence the work reported in this paper.

Acknowledgements

This work was funded by national funds through the Portuguese Foundation for Science and Technology (FCT) under the scope of the FunFibRAI project with reference PTDC/EME-EME/4197/2021 (DOI 10.54499/PTDC/EME-EME/4197/2021). S. Madeira thanks FCT for the contract under the Stimulus of Scientific Employment with reference 2023.08614.CEECIND/CP2841/CT0009 (DOI 10.54499/2023.08614.CEECIND/CP2841/CT0009). This research was also funded by FCT through the reference project UID/04436: CMEMS-UMinho.

References

[1] V.H.S. Tey, R. Phillips, K. Tan, Five-year Retrospective study on success, Survival and incidence of complications of single crowns supported by dental implants, Clin. Oral Implants Res. 28 (2017) 620–625, https://doi.org/10.1111/clr.12843.
[2] M. Durkan, Implant dentistry at a glance, Br. Dent. J. 215 (2013), https://doi.org/10.1038/sj.bdj.2013.1039, 438–438.
[3] J.D. Lin, A.T. Jang, M.P. Kurylo, J. Hurng, F. Yang, L. Yang, A. Pal, L. Chen, S. P. Ho, Periodontal ligament entheses and their adaptive role in the context of dentoalveolar joint function, Dent. Mater. 33 (2017) 650–666.
[4] M. Tsukasaki, N. Komatsu, K. Nagashima, T. Nitta, W. Pluemsakunthai, C. Shukunami, Y. Iwakura, T. Nakashima, K. Okamoto, H. Takayanagi, Host defense against oral microbiota by bone-damaging T cells, Nat. Commun. 9 (2018) 1–11, https://doi.org/10.1038/s41467-018-03147-6.
[5] T. de Jong, A.D. Bakker, V. Everts, T.H. Smit, The intricate anatomy of the periodontal ligament and its development: lessons for periodontal regeneration, J. Periodontal. Res. 52 (2017).
[6] L. Chambrone, L.A. Chambrone, L.A. Lima, Effects of occlusal overload on peri-implant tissue health: a systematic review of animal-model studies, J. Periodontol. 81 (2010) 1367–1378, https://doi.org/10.1902/jop.2010.100176.
[7] A. Alani, M. Kelleher, K. Bishop, Peri-implantitis. Part 1: scope of the problem, Br. Dent. J. 217 (2014) 281–287.
[8] P.J. Tavares Fp, Relation between dental implant joint surfaces and biofilm formation, Dentistry (2015) 05, https://doi.org/10.4172/2161-1122.1000296.
[9] M. Gasik, Understanding biomaterial-tissue interface quality: combined in vitro evaluation, Sci. Technol. Adv. Mater. 18 (2017) 550–562.
[10] A. Miyashita, S. Fukushima, Y. Kokubo, A. Miyashita, S. Oida, K. Komatsu, A. Shimada, S. Shimoda, Effect of remaining periodontal ligament on the healing-up of the implant placement, J. Hard Tissue Biol. 14 (2005) 198–200, https://doi.org/10.2485/jhtb.14.198.
[11] X. Pei, L. Wang, C. Chen, X. Yuan, Q. Wan, J.A. Helms, Contribution of the PDL to osteotomy repair and implant osseointegration, J. Dent. Res. 96 (2017) 909–916, https://doi.org/10.1177/0022034517707513.
[12] Tetè, S.; Mastrangelo, F.; Bianchi, A.; Zizzari, V.; Scarano, A. Collagen fiber orientation around machined titanium and zirconia dental implant necks: an animal study. Int. J. Oral Maxillofac. Implants 24, 52–58.
[13] J. Zhao, L. Faure, I. Adameyko, P.T. Sharpe, Stem cell contributions to cementoblast differentiation in healthy periodontal ligament and periodontitis, Stem Cell. 39 (2021) 92–102, https://doi.org/10.1002/stem.3288.
[14] M.M. Saito, K. Onuma, Y. Yamakoshi, Cementum is key to periodontal tissue regeneration: a review on apatite microstructures for creation of novel cementum-based dental implants, Genes 61 (2023).

[15] B.L. Foster, F.H. Nociti, M.J. Somerman, Development and structure of cementum, in: Dental Cementum in Anthropology, Cambridge University Press, 2022, pp. 46–64.

[16] N. Juntavee, A. Juntavee, P. Plongniras, Remineralization potential of nano-hydroxyapatite on enamel and cementum surrounding margin of computer-aided design and computer-aided manufacturing ceramic restoration, Int. J. Nanomed. 13 (2018) 2755–2765, https://doi.org/10.2147/IJN.S165080.

[17] S. Metwally, U. Stachewicz, Teeth resorption at cement - enamel junction (CEJ) - microscopy analysis, Micron 137 (2020) 102913, https://doi.org/10.1016/j.micron.2020.102913.

[18] K. Sarna-Boś, K. Skic, P. Boguta, A. Adamczuk, M. Vodanovic, R. Chałas, Elemental mapping of human teeth enamel, dentine and cementum in view of their microstructure, Micron 172 (2023), https://doi.org/10.1016/j.micron.2023.103485.

[19] R. He, C. Chou, L. Chen, M. Stoller, M. Kang, S.P. Ho, Insights into pulp biomineralization in human teeth, Front. Dent. Med. 3 (2022) 883336, https://doi.org/10.3389/FDMED.2022.883336/BIBTEX.

[20] R.B. Osman, M.V. Swain, A critical review of dental implant materials with an emphasis on titanium versus zirconia, Materials 8 (2015) 932–958.

[21] K. Shahramian, M. Gasik, I. Kangasniemi, X.F. Walboomers, J. Willberg, A. Abdulmajeed, T. Närhi, Zirconia implants with improved attachment to the gingival tissue, J. Periodontol. 91 (2020) 1213–1224, https://doi.org/10.1002/JPER.19-0323.

[22] J.P. Matinlinna, Handbook of Oral Biomaterials, 2014. ISBN 9789814463133.

[23] A. Zühlke, M. Gasik, K. Shahramian, T. Närhi, Y. Bilotsky, I. Kangasniemi, Enhancement of gingival tissue adherence of zirconia implant posts: in vitro study, Materials 14 (2021) 1–12, https://doi.org/10.3390/ma14020455.

[24] L. Rimondini, M. Gasik, Bacterial attachment and biofilm formation on biomaterials, in: Biomaterials and Immune Response, CRC Press, 2018, pp. 87–120. ISBN 9781315147147.

[25] A. D'Agostino, G. Misiti, A.C. Scalia, M. Pavarini, A. Fiorati, A. Cochis, L. Rimondini, V.F. Borrini, M. Manfredi, L. Andena, et al., Gallium-doped zirconia coatings modulate microbiological outcomes in dental implant surfaces, J. Biomed. Mater. Res., Part A 112 (2024), https://doi.org/10.1002/jbm.a.37727.

[26] M. Pessanha-Andrade, M.B. Sordi, B. Henriques, F.S. Silva, W. Teughels, J.C. M. Souza, Custom-made root-analogue zirconia implants: a scoping review on mechanical and biological benefits, J. Biomed. Mater. Res. Part B Appl. Biomater. 106 (2018) 2888–2900.

[27] T. Dantas, F. Rodrigues, J. Araújo, P. Vaz, F. Silva, Customized root-analogue dental implants - procedure and errors associated with image acquisition, treatment, and manufacturing technology in an experimental study on a cadaver dog mandible, J. Mech. Behav. Biomed. Mater. 133 (2022), https://doi.org/10.1016/j.jmbbm.2022.105350.

[28] T.A. Dantas, J.P. Carneiro Neto, J.L. Alves, P.C.S. Vaz, F.S. Silva, In silico evaluation of the stress fields on the cortical bone surrounding dental implants: comparing root-analogue and screwed implants, J. Mech. Behav. Biomed. Mater. 104 (2020) 103667, https://doi.org/10.1016/j.jmbbm.2020.103667.

[29] J. Chen, Z. Zhang, X. Chen, C. Zhang, G. Zhang, Z. Xu, Design and manufacture of customized dental implants by using reverse engineering and selective laser melting technology, J. Prosthet. Dent 112 (2014) 1088–1095.E1, https://doi.org/10.1016/j.prosdent.2014.04.026.

[30] A. Marques, G. Miranda, D. Faria, P. Pinto, F. Silva, Ó. Carvalho, Novel design of low modulus high strength zirconia scaffolds for biomedical applications, J. Mech. Behav. Biomed. Mater. 97 (2019) 375–384, https://doi.org/10.1016/j.jmbbm.2019.05.005.

[31] X. Luo, J. Niu, G. Su, L. Zhou, X. Zhang, Y. Liu, Q. Wang, N. Sun, Research progress of biomimetic materials in oral medicine, J. Biol. Eng. 17 (2023) 1–24.

[32] N. Nakamura, A. Ito, T. Kimura, A. Kishida, Extracellular matrix induces periodontal ligament reconstruction in vivo, Int. J. Mol. Sci. 20 (2019), https://doi.org/10.3390/ijms20133277.

[33] A.K. Gaharwar, I. Singh, A. Khademhosseini, Engineered biomaterials for in situ tissue regeneration, Nat. Rev. Mater. 5 (2020) 686–705.

[34] J. Hwang, Y. Jeong, J.M. Park, K.H. Lee, J.W. Hong, J. Choi, Biomimetics: forecasting the future of science, engineering, and medicine, Int. J. Nanomed. 10 (2015) 5701–5713.

[35] C.I. Resende-Gonçalves, N. Sampaio, J. Moreira, O. Carvalho, J. Caramês, M. C. Manzanares-Céspedes, F. Silva, B. Henriques, J. Souza, Porous zirconia blocks for bone repair: an integrative review on biological and mechanical outcomes, Ceramics 5 (2022) 161–172.

[36] M.V. Sivasankar, M.L. Chinta, P. Sreenivasa Rao, Zirconia based composite scaffolds and their application in bone tissue engineering, Int. J. Biol. Macromol. 265 (2024) 130558.

[37] I.N. Safi, B.M.A. Hussein, A.M. Al-Shammari, Bio-hybrid dental implants prepared using stem cells with β-TCP-coated titanium and zirconia, J. Periodontal Implant Sci. 52 (2022), https://doi.org/10.5051/JPIS.2006080304.

[38] M. Yamada, T. Kimura, N. Nakamura, J. Watanabe, N. Kartikasari, X. He, W. Tiskratok, H. Yoshioka, H. Shinno, H. Egusa, Titanium nanosurface with a biomimetic physical microenvironment to induce endogenous regeneration of the periodontium, ACS Appl. Mater. Interfaces 14 (2022) 27703–27719, https://doi.org/10.1021/acsami.2c06679.

[39] Dr T. Kano, R. Yamamoto, A. Miyashita, K. Komatsu, T. Hayakawa, M. Sato, S. Oida, Regeneration of periodontal ligament for apatite-coated tooth-shaped titanium implants with and without occlusion using rat molar model, J. Hard Tissue Biol. 21 (2012) 189–202, https://doi.org/10.2485/jhtb.21.189.

[40] S. Sowmya, U. Mony, P. Jayachandran, S. Reshma, R.A. Kumar, H. Arzate, S. V. Nair, R. Jayakumar, Tri-layered nanocomposite hydrogel scaffold for the concurrent regeneration of cementum, periodontal ligament, and alveolar bone, Adv. Healthcare Mater. 6 (2017) 1601251, https://doi.org/10.1002/ADHM.201601251.

[41] C.H. Lee, J. Hajibandeh, T. Suzuki, A. Fan, P. Shang, J.J. Mao, Three-dimensional printed multiphase scaffolds for regeneration of periodontium complex, Tissue Eng. 20 (2014) 1342–1351, https://doi.org/10.1089/ten.tea.2013.0386.

[42] K. Kim, C.H. Lee, B.K. Kim, J.J. Mao, Anatomically shaped tooth and periodontal regeneration by cell homing, J. Dent. Res. 89 (2010) 842–847, https://doi.org/10.1177/0022034510370803.

[43] D. Faria, B. Henriques, D. Fabris, L. Grémillard, O. Carvalho, F.S. Silva, J. Mesquita-Guimarães, Enhancing hydrothermal degradation resistance of (3Y, 12Ce)-TZP composites for biomedical applications: a design perspective, Ceram. Int. 51 (2025) 19598–19609, https://doi.org/10.1016/J.CERAMINT.2025.02.135.

[44] M.F.R.P. Alves, L.Q.B. de Campos, B.G. Simba, C.R.M. da Silva, K. Strecker, C. dos Santos, Microstructural characteristics of 3Y-tzp ceramics and their effects on the flexural strength, Ceramics 5 (2022) 798–813, https://doi.org/10.3390/ceramics5040058.

[45] S. Roedel, J. Mesquita-Guimarães, J.C.M. Souza, F.S. Silva, M.C. Fredel, B. Henriques, Production and characterization of zirconia structures with a porous surface, Mater. Sci. Eng. C 101 (2019) 264–273, https://doi.org/10.1016/j.msec.2019.03.087.

[46] S.S. Scherrer, M. Cattani-Lorente, E. Vittecoq, F. De Mestral, J.A. Griggs, H.W. A. Wiskott, Fatigue behavior in water of Y-tzp zirconia ceramics after abrasion with 30 Mm silica-coated alumina particles, Dent. Mater. 27 (2011), https://doi.org/10.1016/j.dental.2010.10.003.

[47] S. Madeira, J. Mesquita-Guimarães, P. Ribeiro, M. Fredel, J.C.M. Souza, D. Soares, F.S. Silva, B.Y.- Henriques, TZP/Porcelain graded dental restorations design for improved damping behavior – a study on damping capacity and dynamic young's modulus, J. Mech. Behav. Biomed. Mater. 96 (2019) 219–226, https://doi.org/10.1016/j.jmbbm.2019.04.033.

[48] F. Rupp, R.A. Gittens, L. Scheideler, A. Marmur, B.D. Boyan, Z. Schwartz, J. Geis-Gerstorfer, A review on the wettability of dental implant surfaces I: theoretical and experimental aspects, Acta Biomater. 10 (2014) 2894–2906.

[49] A. Moreira, S. Madeira, M. Buciumeanu, J. Fialho, A. Carvalho, F. Silva, F. J. Monteiro, J. Caramês, Design and surface characterization of micropatterned silica coatings for zirconia dental implants, J. Mech. Behav. Biomed. Mater. 126 (2022), https://doi.org/10.1016/j.jmbbm.2021.105060.

[50] N. Nicklisch, C. Hinrichs, L. Palaske, W. Vach, K.W. Alt, Variability in human tooth cementum thickness reflecting functional processes, J. Periodontal. Res. 59 (2024) 408–419, https://doi.org/10.1111/jre.13226.

[51] J.L. Hernandez, K.A. Woodrow, Medical applications of porous biomaterials: features of porosity and tissue-specific implications for biocompatibility, Adv. Healthcare Mater. 11 (2022) e2102087.

[52] B. Coppola, L. Montanaro, P. Palmero, DLP fabrication of zirconia scaffolds coated with HA/β-TCP layer: role of scaffold architecture on mechanical and biological properties, J. Funct. Biomater. 13 (2022), https://doi.org/10.3390/jfb13030148.

[53] C.L. Gnanasagaran, K. Ramachandran, N.H. Jamadon, V.H. Kumar, A. Muchtar, A. Pazhani, B. Ayaz, Microstructural and mechanical behaviours of Y-tzp prepared via slip-casting and fused deposition modelling (FDM), Heliyon 9 (2023) e21705, https://doi.org/10.1016/j.heliyon.2023.e21705.

[54] E. Vennat, C. Bogicevic, J.M. Fleureau, M. Degrange, Demineralized dentin 3D porosity and pore size distribution using mercury porosimetry, Dent. Mater. 25 (2009) 729–735, https://doi.org/10.1016/j.dental.2008.12.002.

[55] C.H. Park, J.H. Oh, H.M. Jung, Y. Choi, S.U. Rahman, S. Kim, T. Il Kim, H.I. Shin, Y. S. Lee, F.H. Yu, et al., Effects of the incorporation of ε-aminocaproic acid/chitosan particles to fibrin on cementoblast differentiation and cementum regeneration, Acta Biomater. 61 (2017) 134–143, https://doi.org/10.1016/j.actbio.2017.07.039.

[56] B. Guimarães, D. Figueiredo, C.M. Fernandes, F.S. Silva, G. Miranda, O. Carvalho, Laser machining of WC-Co green compacts for cutting tools manufacturing, Int. J. Refract. Met. Hard Mater. 81 (2019) 316–324, https://doi.org/10.1016/j.ijrmhm.2019.03.018.

[57] D. Faria, S. Madeira, M. Buciumeanu, F.S. Silva, O. Carvalho, Novel laser textured surface designs for improved zirconia implants performance, Mater. Sci. Eng. C 108 (2020) 110390, https://doi.org/10.1016/j.msec.2019.110390.

[58] A. Zareidoost, M. Yousefpour, B. Ghasemi, A. Amanzadeh, The relationship of surface roughness and cell response of chemical surface modification of titanium, J. Mater. Sci. Mater. Med. 23 (2012) 1479–1488, https://doi.org/10.1007/s10856-012-4611-9.

[59] A. Pae, H. Lee, H.S. Kim, Y.D. Kwon, Y.H. Woo, Attachment and growth behaviour of human gingival fibroblasts on titanium and zirconia ceramic surfaces, Biomed. Mater. 4 (2009) 025005, https://doi.org/10.1088/1748-6041/4/2/025005.

[60] W.M.S. Al Qahtani, C. Schille, S. Spintzyk, M.S.A. Al Qahtani, E. Engel, J. Geis-Gerstorfer, F. Rupp, L. Scheideler, Effect of surface modification of zirconia on cell adhesion, metabolic activity and proliferation of human osteoblasts, Biomed. Tech. 62 (2017) 75–87, https://doi.org/10.1515/bmt-2015-0139.

[61] J. Drelich, A. Marmur, Physics and applications of superhydrophobic and superhydrophilic surfaces and coatings, Surf. Innovations 2 (2014) 211–227, https://doi.org/10.1680/si.13.00017.

[62] C.G. Moura, R. Pereira, M. Buciumeanu, O. Carvalho, F. Bartolomeu, R. Nascimento, F.S. Silva, Effect of laser surface texturing on primary stability and surface properties of zirconia implants, Ceram. Int. 43 (2017) 15227–15236, https://doi.org/10.1016/j.ceramint.2017.08.058.

[63] T. Dantas, J. Padrão, M.R. da Silva, P. Pinto, S. Madeira, P. Vaz, A. Zille, F. Silva, Bacteria Co-culture adhesion on different texturized zirconia surfaces, J. Mech.

Behav. Biomed. Mater. 123 (2021), https://doi.org/10.1016/j.jmbbm.2021.104786.
[64] J.H.C. de Lima, P.C.M. Robbs, E.M.O. Tude, P.N. De Aza, E.M. da Costa, A. Scarano, J.C. Prados-Frutos, G.V.O. Fernandes, S.A. Gehrke, Fibroblasts and osteoblasts behavior after contact with different titanium surfaces used as implant abutment: an in vitro experimental study, Heliyon 10 (2024) e25038, https://doi.org/10.1016/J.HELIYON.2024.E25038.
[65] C. Wang, X. Wang, R. Lu, X. Cao, D. Yuan, S. Chen, Influence of surface nanotopography and wettability on early phases of peri-implant soft tissue healing: an in-vivo study in dogs, BMC Oral Health 23 (2023) 1–12, https://doi.org/10.1186/s12903-023-03347-7.
[66] M.T. Matter, L. Maliqi, K. Keevend, S. Guimond, J. Ng, E. Armagan, M. Rottmar, I. K. Herrmann, One-step synthesis of versatile antimicrobial nano-architected implant coatings for hard and soft tissue healing, ACS Appl. Mater. Interfaces 13 (2021) 33300–33310, https://doi.org/10.1021/acsami.1c10121.
[67] T.A. Dantas, P. Pinto, P.C.S. Vaz, F.S. Silva, Design and optimization of zirconia functional surfaces for dental implants applications, Ceram. Int. 46 (2020) 16328–16336, https://doi.org/10.1016/j.ceramint.2020.03.190.
[68] A. Barone, F. Alfonsi, G. Derchi, P. Tonelli, P. Toti, S. Marchionni, U. Covani, The effect of insertion torque on the clinical outcome of single implants: a randomized clinical trial, Clin. Implant Dent. Relat. Res. 18 (2016) 588–600, https://doi.org/10.1111/cid.12337.
[69] J. Rozlivka, V. Kaśpar, P. Dostál, M. Černe, B. Hajtman, J. Žarnovske, Using acoustic emission for measuring surface roughness, Acta Technol. Agric. 23 (2020) 150–154, https://doi.org/10.2478/ata-2020-0024.
[70] D.K. Das, M.P. Srivastava, S.V. Joshi, R. Sivakumar, Scratch adhesion testing of plasma-sprayed yttria-stabilized zirconia coatings, Surf. Coating. Technol. 46 (1991) 331–345, https://doi.org/10.1016/0257-8972(91)90175-V.
[71] S. Madeira, M. Buciumeanu, D. Nobre, O. Carvalho, F.S. Silva, Development of a novel hybrid Ti6Al4V–ZrO2 surface with high wear resistance by laser and hot pressing techniques for dental implants, J. Mech. Behav. Biomed. Mater. 136 (2022) 105508, https://doi.org/10.1016/j.jmbbm.2022.105508.